

Plume Migration of Different Carbon Dioxide Phases During Geological Storage in Deep Saline Aquifers

Chien-Hao Shen¹, Long Nghiem², Ta-Lin Chen³, and Bieng-Zih Hsieh^{1,*}

¹Department of Resources Engineering, National Cheng Kung University, Tainan, Taiwan, R.O.C.

²Computer Modelling Group Ltd., Alberta, Canada

³Exploration and Development Research Institute, CPC Corporation, Miaoli, Taiwan, R.O.C.

Received 30 April 2014, revised 5 August 2014, accepted 5 January 2015

ABSTRACT

This study estimates the plume migration of mobile supercritical phase (flowing), aqueous phase (dissolved), and ionic phase CO₂ (bicarbonate), and evaluates the spatial distribution of immobile supercritical phase (residual) and mineral phase CO₂ (carbonates) when CO₂ was sequestered. This utilized a simulation, in an anticline structure of a deep saline aquifer in the Tiechenshan (TCS) field, Taiwan. All of the trapping mechanisms and different CO₂ phases were studied using the fully coupled geochemical equation-of-state GEM compositional simulator. The mobile supercritical phase CO₂ moved upward and then accumulated in the up-dip of the structure because of buoyancy. A large amount of immobile supercritical phase CO₂ was formed at the rear of the moving plume where the imbibition process prevailed. Both the aqueous and ionic phase CO₂ finally accumulated in the down-dip of the structure because of convection. The plume volume of aqueous phase CO₂ was larger than that of the supercritical phase CO₂, because the convection process increased vertical sweep efficiency. The up-dip of the structure was not the major location for mineralization, which is different from mobile supercritical phase CO₂ accumulation.

Key words: Carbon dioxide storage, Deep saline aquifer, Numerical simulation, Plume migration, Trapping mechanism

Citation: Shen, C. H., L. Nghiem, T. L. Chen, and B. Z. Hsieh, 2015: Plume migration of different of carbon dioxide phases during geological storage in deep saline aquifers. *Terr. Atmos. Ocean. Sci.*, 26, 375-386, doi: 10.3319/TAO.2015.01.05.02(TT)

1. INTRODUCTION

Storing carbon dioxide (CO₂) geologically is a technology that benefits from extensive petroleum engineering experience from dealing with hydrocarbon production and storing natural gas (IPCC 2005; IEA 2008). Suitable formations for CO₂ storage include depleted oil and gas reservoirs, coal seams, and saline aquifers. Compared with other geological media, deep saline aquifers have the largest storage capacity and can be found in most of the world's sedimentary basins. This is an advantage in terms of CO₂ transport from emission sources (IPCC 2005; Bachu 2008).

Several trapping mechanisms act to prevent the buoyant CO₂ from coming back to the atmosphere when CO₂ is stored in a saline aquifer. These mechanisms include stratigraphic and structural, residual gas, solubility, ionic, and mineral trappings (Pruess et al. 2003; Nghiem et al. 2004, 2009a, b; Kumar et al. 2005; Bachu 2008). Corresponding-

ly, CO₂ mobile and immobile supercritical, aqueous, ionic, and mineral phases exist simultaneously in the aquifer.

When stored in a saline aquifer, CO₂ is always less dense and less viscous than the groundwater, making it buoyant and mobile in the aquifer (Bachu 2003). The mobile supercritical CO₂ plume will migrate upward, under the impermeable cap rock (Bachu 2008). Over time, other and more secure trapping mechanisms take over. In residual gas trapping, the CO₂ is trapped in the rock pore space by capillary pressure (Flett et al. 2004; Bennion and Bachu 2005; Kumar et al. 2005; Juanes et al. 2006; Ide et al. 2007; Bachu 2008; Nghiem et al. 2009a, b, c; Qi et al. 2009). There is no "plume migration" in immobile supercritical phase (residual) CO₂ because it is trapped and fixed in the rock pores. The "spatial distribution" of immobile supercritical phase (residual) CO₂ is investigated in this study.

Much of the injected CO₂ will eventually dissolve into the saline water. This process, which further traps the CO₂, is called solubility trapping (Kumar et al. 2005; Bachu

* Corresponding author
E-mail: bzhsieh@mail.ncku.edu.tw

2008; Nghiem et al. 2009a, b, c). The plume migration of the dissolved CO₂ (or aqueous phase CO₂) is different from that of mobile supercritical CO₂, because solubility trapping forms a denser fluid and causes a concentration difference in the saline water, which may then sink to the bottom of the formation (Ennis-King and Paterson 2005).

The dissolved CO₂ reacts with formation water and then dissociates into bicarbonate (HCO₃⁻) and carbonate (CO₃²⁻) ions. This chemical reaction is the ionic trapping mechanism (Gunter et al. 2004; Kumar et al. 2005; Bachu 2008; Nghiem et al. 2009a, b). The dissociated bicarbonate ions are referred to as ionic phase CO₂ in this study. The plume migration might be similar to that of aqueous CO₂ because the ionic phase CO₂ is formed from the existing aqueous phase CO₂.

Depending on the rock formation, the ionic CO₂ may react chemically with the surrounding rocks to form stable minerals. Known as mineral trapping, this process can store CO₂ permanently and provides the most secure form of storage for the CO₂ (Bachu et al. 1994; Gunter et al. 1997, 2004, 2008; Nghiem et al. 2004, 2009a, b; Rochelle et al. 2004; Xu et al. 2004; Gaus et al. 2005; Thibeau et al. 2007; Bachu 2008). Similar to residual CO₂, there is no plume migration in the mineral phase CO₂ (i.e., carbonates) because it is precipitated or bound to the rock matrix. The “spatial distribution” of the mineral (solid) phase CO₂ is investigated here.

The plume migration and the spatial distribution of different of CO₂ phases provide essential information for monitoring, risk assessment, and management issues when a CO₂ storage project is developed. The U.S. Environmental Protection Agency (EPA) Underground Injection Control Program requires that the permit applicant define an Area of Review (AOR) in which all penetrations intersecting the injection formation or its confining layer be identified and be determined to have been properly plugged and abandoned when a proposed injection operation has the potential for contaminating underground sources of drinking water through wells, faults or other pathways that penetrate an injection zone (Nicot et al. 2008; EPA 2014). The AOR for a CO₂ storage project should be defined and investigated before CO₂ is injected into a reservoir. The AOR is traditionally evaluated from the plume migration of mobile supercritical CO₂ phase. The integrated AOR evaluation should include all CO₂ phase because different CO₂ phases have different migration behaviors.

A CO₂ storage project is currently preparing to launch in Taiwan. An onshore saline aquifer of the Yutengping sandstone formation in the Tiechenshan (TCS) field in northwestern Taiwan is a potential site for this project. This study evaluates the AOR from the plume migration of mobile supercritical, aqueous, and ionic CO₂, and from the spatial distribution of the immobile supercritical and mineral phase CO₂ when CO₂ is stored in the anticline structure of a deep saline aquifer in the TCS field.

2. CO₂ TRAPPING MECHANISMS AND PLUME MIGRATION

2.1 Structural Trapping

The critical pressure and critical temperature of CO₂ are 7376 kPa and 304.2 K (31°C), respectively. When CO₂ is injected into an aquifer deeper than 800 m, it is in a supercritical state (Bachu 2003). The density of the injected supercritical CO₂ is approximately 5160 kg m⁻³ (or 32.9 lb ft⁻³) at reservoir conditions of 16858 kPa (or 2445 psi) and 72.2°C (or 162°F), which is lower than that of saline formation water (10039 kg m⁻³ or 63.9 lb ft⁻³ at the same reservoir conditions). The flow behavior of supercritical CO₂ in an aquifer is similar to that of a fluid (Nghiem et al. 2009a, b). Buoyancy drives the injected CO₂ to migrate upward until an impermeable cap rock traps it. Thus, the structural trapping mechanism needs a cap rock to prevent mobile CO₂ from leaking out of the storage reservoir (Bachu 2008).

2.2 Residual Gas Trapping

Residual gas trapping is the one of the important processes for trapping CO₂. The mechanism converts CO₂ into an immobile phase in the pores via the capillary effect and imbibition. The imbibition usually occurs at the rear of the plume of supercritical CO₂ after the injection stops. The classic Land's model (Land 1968) (Fig. 1) was used in this study to calculate the residual gas (CO₂) saturation [Eqs. (1) and (2)], as follows (Nghiem et al. 2009a, b):

$$S_{gt}^*(S_{gi}^*) = \frac{S_{gi}^*}{1 + CS_{gi}^*} \quad (1)$$

$$C = \frac{1}{S_{gt, \max}} - \frac{1}{S_{g, \max}} \quad (2)$$

where S_{gt}^* = residual gas saturation corresponding to S_{gi}^* , S_{gi}^* = the gas saturation value (S_g) when the shift to imbibition

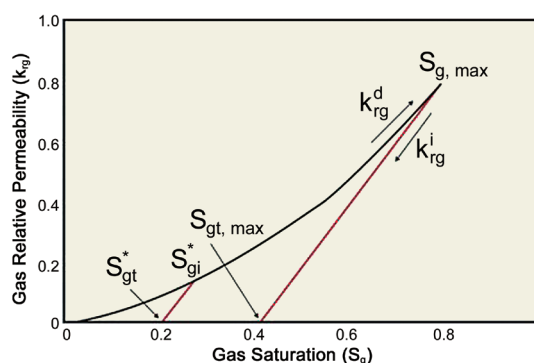


Fig. 1. The Land's residual gas trapping model (Nghiem et al. 2009a). The maximum residual gas saturation is 0.4.

occurs. C = Land's coefficient, $S_{g, \max}$ = the maximum gas saturation, $S_{gr, \max}$ = the maximum residual gas saturation.

When the gas saturation S_{gi}^* reverses and decreases at drainage curve, the gas relative permeability follows the imbibition curve k_{rg}^i (red curve).

2.3 Solubility Trapping

Solubility trapping causes both mobile and immobile supercritical CO₂ to change into an aqueous phase via the dissolution process. Denser CO₂-saturated water will be formed and it will tend to sink to the bottom of the formation. The convection effect will force the fresh water to replace the CO₂-saturated water. Consequently, more supercritical CO₂ dissolves into the water.

CO₂ solubility in brine can be modeled as a phase-equilibrium process. To calculate the quantity of aqueous CO₂, the equality of fugacities in the gas and aqueous phase used is as follows (Nghiem et al. 2009a, b):

$$f_{\text{CO}_2, g} = f_{\text{CO}_2, aq} \quad (3)$$

In this study, the fugacity of CO₂ in the gas phase ($f_{\text{CO}_2, g}$) was calculated using the Peng-Robinson equation-of-state (EOS) (Peng and Robinson 1976), and the fugacity of CO₂ in the aqueous phase ($f_{\text{CO}_2, aq}$) was modeled with Henry's law (Li and Nghiem 1986), as follows:

$$f_{\text{CO}_2, aq} = y_{\text{CO}_2, aq} \cdot H_{\text{CO}_2} \quad (4)$$

where $y_{\text{CO}_2, aq}$ = the mole fraction of CO₂ in the aqueous phase and H_{CO_2} = Henry's constant of CO₂, which is a function of pressure, temperature and salinity.

Gas solubility increases with increasing pressure and decreases with increasing temperature or salinity (Nghiem et al. 2009a, b). The correlations derived by Harvey (1996), Garcia (2001), and Bakker (2003) are used to obtain an accurate prediction of CO₂ solubility in water (Nghiem et al. 2009a, b; CMG 2011a).

2.4 Ionic Trapping

The H⁺ and HCO₃⁻ or CO₃²⁻ ions are dissociated when the injected CO₂ dissolves in water. The main chemical reactions related to CO₂ sequestration are as follows:



where CO_{2(aq)} = the CO₂ that is dissolved in the aqueous phase (from solubility trapping).

Chemical equilibrium reactions were used in this study to model this fast and reversible intra-aqueous chemical reaction (ionic trapping mechanism) (Nghiem et al. 2009a, b). The chemical equilibrium reactions were governed by chemical equilibrium constants (Bethke 1996; Nghiem et al. 2009a, b), as follows:

$$Q_\alpha - K_{eq, \alpha} = 0, \quad \alpha = 1, \dots, R_{aq} \quad (7)$$

where R_{aq} = the number of intra-aqueous chemical equilibrium reactions, $K_{eq, \alpha}$ = the chemical equilibrium constant for the aqueous reaction α , and Q_α = the activity product for the aqueous reaction α .

The values of $K_{eq, \alpha}$ for several aqueous reactions were studied by Kharaka et al. (1988) and Delaney and Lundeen (1990). The activity product (Q_α) is calculated by (Nghiem et al. 2009a, b):

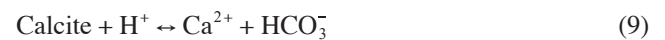
$$Q_\alpha = \prod_{k=1}^{n_{aq}} a_k^{v_{k, \alpha}} \quad (8)$$

where n_{aq} = the number of aqueous components, a_k = the activity of component k , and $v_{k, \alpha}$ = the stoichiometry coefficients of the chemical equilibrium reactions.

The activities a_k are the product of the molality (m_k , moles per kg of H₂O) and the activity coefficient (γ_k) of component k . An efficient model for calculating the ionic activity coefficients is the *B-dot* model for the non-ideal solution (Bethke 1996) or the Pitzer (1987) model for a high-salinity solution (Nghiem et al. 2009a, b).

2.5 Mineral Trapping

The ions that are dissociated through the chemical equilibrium reaction will react with the minerals in place, and with other ions in the solution, and will lead to the precipitation of carbonate minerals or the dissolution of formation minerals. The typical geochemical reaction for the precipitation or dissolution of calcite (CaCO₃) is:



Geochemical reactions occur between minerals and aqueous components, and are reversible. The dissolution or precipitation of minerals follows the reaction rate (r_β), given by (Bethke 1996; Nghiem et al. 2009a, b):

$$r_\beta = \hat{A}_\beta k_\beta \left(1 - \frac{Q_\beta}{K_{eq, \beta}} \right), \quad \beta = 1, \dots, R_{mn} \quad (10)$$

where r_β = the reaction rate for a given mineral β , R_{mn} = the number of mineral reactions, \hat{A}_β = the reactive surface

area, k_{β} = the rate constant of the mineral reaction, $K_{eq, \beta}$ = the chemical equilibrium constant of the mineral reaction, and Q_{β} = the activity product of the mineral reaction.

The ratio of the activity product to the chemical equilibrium constant ($Q_{\beta}/K_{eq, \beta}$) is the saturation index (SI) of the reaction and is used to evaluate the dissolution or precipitation path (Nghiem et al. 2009a, b). The changes in the moles of minerals through dissolution or precipitation can be estimated after the geochemical reaction occurs.

3. GEOLOGICAL SETTING AND ENGINEERING DATA

This case study area is located in the Taihsi basin, in northwest Taiwan. The Taihsi basin is situated near the Taiwan mountain ranges with the eastern boundary of the deformation front (Fig. 2). To the North and South, the Taihsi basin is bounded by the Kuanyin uplift and Penghu platform, respectively (Fig. 2). The west of the Taihsi basin connects with the Taiwan Strait shelf. The thickness of the Taihsi basin is about 8 km. The formation dip angle is about 4° from west to east, which is caused by the orogenic load of the Taiwan mountain ranges (Lin 2001; Lin et al. 2003).

The Cenozoic sediments of the Taihsi basin, which have the highest capacity for CO₂ storage in Taiwan (Lin 2007), can be divided by three evolution episodes: the Paleocene-Eocene syn-rift, the Oligocene-Miocene post-breakup, and the Latest Miocene-Recent foreland basin (Lin et al. 2003). The sedimentary formations in the Oligocene-Miocene post-breakup period, from bottom to top, are the Wuchihshan, Mushan, Piling, Shihti, and Nankang formations, which are the major gas reservoirs and hydrocarbon source rocks in Taiwan (Fig. 3). The sedimentary formations in the latest Miocene-Recent foreland basin are the Kueichulin, Chinshui, Cholan, and Toukoshan formations, which are saline aquifers (Fig. 3).

The Kueichulin formation was selected for the CO₂ storage project in the Taihsi basin, because its depth interval is suitable for the storage of CO₂ in its supercritical state (Bachu 2003; Lin 2007). The Kueichulin formation is divided into three parts: Yutengping sandstone, Shihliufen shale, and Kuantaoshan sandstone (Fig. 3). The Yutengping sandstone is the top layer and is overlain by the impermeable Chinshui shale (Fig. 3). The thickness of the Chinshui shale is approximately 300 m and its permeability is extremely low, less than 10⁻⁴ md. The Chinshui shale is the caprock and will prevent CO₂ leakage after CO₂ has been injected into the Yutengping sandstone for storage. The Yutengping sandstone lies on top of the Shihliufen shale, which is treated as the impermeable lower boundary of the CO₂ storage formation.

The selected potential storage site is an anticline trap with a closure depth of 1600 m (Fig. 4). The formation parameters of Yutengping sandstone (Table 1) were collected from the available drilling reports, core analyses, and well

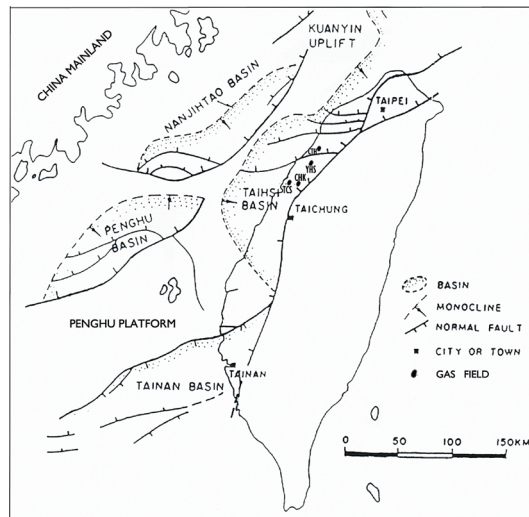


Fig. 2. Location of the Taihsi basin. The black dots show the location of major gas fields (based on Hsieh et al. 2013).

Era	Period	Epoch	Geologic Age (ma)	Formation/Member	Dominant Lithology		
Cenozoic	Quaternary	Pleistocene	0.2				
			0.48				
			0.9	Toukoshan	Sandstone		
			1.2				
	Tertiary	Neogene	Pliocene	1.8	Cholan	Shale	
				3.0	Chinshui	Shale	
				4.0	Kueichulin	Yutengping	Sandstone
				4.4		Shihliufen	Shale
			Miocene	Late	5.0	Kuentaoshan	Sandstone
					5.6		
			Paleogene	Middle	7.0	Nanchuang	Sandstone
					11.0		
		Early		13.4	Nankang	Kuanyinshan	Sandstone
				14.0		Talu	Shale
		Paleocene	Late	15.0	Pelliao	Sandstone	
				17.0			
			Early	18.0	Shihti	Sandstone	
				21.0	Piling	Shale	
		Mesozoic	Cretaceous	Late	23.0	Mushan	Sandstone
					25.0	Wuchihshan	Shale
26.0							
34.0							
34.5							
38.0							
53.5							
65.0							

Fig. 3. Stratigraphic nomenclature and lithology of the sedimentary succession in the Taihsi basin (after Shaw 1996; Wu et al. 2005).

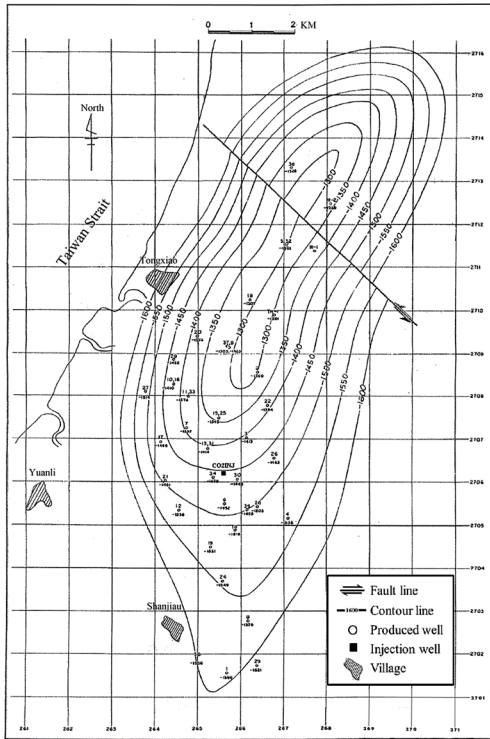


Fig. 4. Anticline structure map of the Yutengping sandstone formation in the TCS field (based on CPC 2010).

Table 1. Basic parameters of the Yutengping sandstone formation.

Parameter (unit)	Value
Formation Top (m)	1300 - 1600
Reservoir Size (m ²)	6.65E7
Grid size (m ³)	228.6 × 228.6 × 41
Porosity (frac.)	0.2
Thickness (m)	205
Permeability (md) ^a	300
Horizontal to Vertical Permeability Ratio	1
Initial Pressure (MPa)	15.7
Reference Depth for Initial Pressure (m)	1547
Temperature (°C)	72
Maximum Gas Saturation (frac.)	0.8
Maximum Residual Gas Saturation (frac.)	0.4
Salinity of the Formation Water Fluid (ppm)	16000

Note: $a: md \times 9.869E - 16 = m^2$.

logging interpretations from Taiwan's CPC Corporation.

Formation water samples from the Yutengping sandstone were laboratory analyzed and their composition Table 2 was corrected using a geochemical aqueous equilibrium model, *Solmineq.88* (Kharaka et al. 1988; GAMS 2011b). XRF (X-ray fluorescence) and XRD (X-ray diffraction) were used to analyze the volume percentage of rock

minerals (Table 3) was analyzed from a formation rock sample.

A geochemical reaction path model, *GAMSPATH* (GAMS 2011a), was used to analyze the intra-aqueous chemical reactions and geochemical reaction paths of rock-brine-CO₂ in a preliminary theoretical study, in which the injection of CO₂ into brine was simulated. The aqueous phase CO₂ [CO_{2(aq)}] was formed and the bicarbonate (HCO₃⁻) ions were then dissociated in the solution. Consequently, the pH value of the solution was lowered. This caused variations in the kaolinite and muscovite early in the simulated period. A small amount of muscovite was dissolved and kaolinite was precipitated. However, anorthite was dissolved continuously in the low pH solution, which dissociated the calcium (Ca²⁺) and aluminum (Al³⁺) in the solution. The reaction between the bicarbonate (HCO₃⁻) and calcium (Ca²⁺) finally led to the precipitation of calcite (CaCO₃). Kaolinite, another secondary mineral, was precipitated because of the dissociated aluminum (Al³⁺). Based on the geochemical reaction analysis result we concluded that there were ten rock-brine-CO₂ interactions: five intra-aqueous chemical reactions in the aqueous phase and five geochemical mineral reactions in the mineral phase (Table 4).

4. RESERVOIR SIMULATION MODEL CONSTRUCTION

The numerical simulation method was used in this study to estimate the plume migration of the supercritical, dissolved, and ionic CO₂ to evaluate the spatial distribution of the residually and mineralogically trapped CO₂ in a saline aquifer. The fully coupled geochemical equation-of-state model (GEM) simulator was used with the GEM-GHG module, a commercial reservoir simulator developed by CMG (Computer Modelling Group Ltd.), which is capable of modeling all trapping mechanisms (Nghiem et al. 2009a, b; CMG 2011a).

The numerical geological model was constructed by dividing the structure into 6365 grids and assuming an open boundary on the edge grid. Each grid is uniform in size (about 228.6 × 228.6 × 41 m), and we divided the reservoir into 5 layers to illustrate the vertical migration path. The rock and fluid properties (formation parameters, fluid PVT data, and relative permeability curves) and formation initial conditions (initial formation pressure, reservoir temperature, formation water analysis data, and rock mineral compositions) were sequentially assigned to each grid block. The specific operation (by designing injection rates or injection pressures) and completion (perforation intervals) conditions were then used to create a model of a well for injecting CO₂ into the aquifer.

To simulate the residual gas trapping, the maximum gas saturation ($S_{g, max}$) and maximum residual gas saturation ($S_{gr, max}$) (Table 1) were used to calculate the Land's

coefficient (C) [Eq. (2)] and to estimate the residual gas saturation (S_{gr}^*) from the Land's model [Eq. (1)]. The hysteresis effect on the gas relative permeability was modeled. The solubility trapping mechanism was modeled from the phase-equilibrium process (Nghiem et al. 2009a, b). The Peng-Robinson EOS and Henry's law parameters, which were used to calculate the fugacities of CO₂ in the gas and aqueous phases, were derived from a phase property program: *WinProp* (CMG 2011b).

This case study was simulated to inject one million tons of CO₂ per year, to create a commercial site for CO₂ storage, with an injection period of 20 years, to create an oil development project life cycle, under the constraint of injection pressure lower than the fracture pressure, for the case of a vertical well at the down-dip of an anticline structure. The total simulation period for studying the plume migration and spatial distribution of the different phases of CO₂ at various times was 1000 years.

5. RESULTS

When CO₂ is injected into an aquifer, the plume of supercritical CO₂ tends to move upward because of the CO₂ buoyant force (Figs. 5a, b). Consequently, the plume is stopped by the cap rock because the cap rock is impermeable. Supercritical CO₂ then flows under the cap rock, following the structure inclination and migrating to the structure up-dip (Fig. 5c).

In the post-injection period, the supercritical CO₂ continuously migrates to the structure up-dip and accumulates in the trap (Fig. 5d). Some supercritical CO₂ is trapped in the pores and becomes immobile at the rear of the moving plume. Solubility trapping also reduces the size of the supercritical CO₂ plume phase, especially in the area of the immobile supercritical CO₂ (Figs. 5e, f).

During CO₂ injection period supercritical CO₂ is continuously injected into the aquifer to drain the formation water away from the wellbore. In this drainage process, there is no residual CO₂ (or immobile supercritical CO₂) formed (Figs. 6a, b). At the end of the injection period, a few pockets of residual CO₂ are formed around the rear side of the plume (Fig. 6c).

In the post-injection period, supercritical CO₂ is no longer injected and imbibition occurs. Residually trapped CO₂ is formed behind the moving supercritical CO₂ plume (Fig. 6d). The amount of residual CO₂ reaches a maximum at the simulation time of 100 years (80 years after the end of CO₂ injection). The solubility trapping mechanism then works to reduce the immobile supercritical CO₂ volume because the trapped CO₂ dissolves into the water (Fig. 6e). At the simulation time of 1000 years, the greater part of the immobile supercritical CO₂ is dissolved into the formation water (Fig. 6f).

The simulation results show that the residual gas trap-

ping mechanism is a fast and safe mechanism in the post-injection period because it fixes a great deal of mobile supercritical CO₂ and provides a good environment for the solubility trapping mechanism to operate.

When mobile or immobile supercritical CO₂ contacts the formation water, CO₂ dissolves into the water and aqueous CO₂ forms. The simulation results show that the aqueous plume migration CO₂ (Figs. 7a - c) is similar to that of supercritical CO₂ (Figs. 5a - c) in a 20-year injection period. However, the aqueous CO₂ plume size is larger than that of supercritical CO₂ because of the convection effect. Because CO₂-saturated water is heavier than the original formation water, it tends to sink to the bottom of the formation (Figs. 7a - c), while the supercritical CO₂ tends to move

Table 2. Aqueous composition reported for the Yutengping sandstone.

Species	Molality (mol kg ⁻¹)
H ⁺	2.64E - 09
Al ³⁺	2.32E - 11
Ca ²⁺	5.46E - 05
SiO _{2(aq)}	2.38E - 04
K ⁺	2.85E - 04
HCO ₃ ⁻	1.27E - 02
CO ₃ ²⁻	9.83E - 04

Table 3. Volume percentage of minerals of formation rock.

Mineral	Volume percentage
Quartz (SiO ₂)	95.6%
Anorthite (CaAl ₂ Si ₂ O ₈)	1.1%
Kaolinite (Al ₂ Si ₂ O ₅ (OH) ₄)	2.3%
Muscovite [KAl ₃ Si ₃ O ₁₀ (OH) ₂]	1.0%

Table 4. Major intra-aqueous chemical reactions and geochemical mineral reactions considered in this study.

Major reactions
Intra-aqueous chemical reactions
CO _{2(aq)} + H ₂ O ↔ H ⁺ + HCO ₃ ⁻
CO ₃ ²⁻ + H ⁺ ↔ HCO ₃ ⁻
OH ⁻ + H ⁺ ↔ H ₂ O
Al(OH) ²⁺ + H ⁺ ↔ Al ³⁺ + H ₂ O
KOH + H ⁺ ↔ K ⁺ + H ₂ O
Geochemical mineral reactions
Calcite + H ⁺ ↔ Ca ²⁺ + HCO ₃ ⁻
Anorthite + 8H ⁺ ↔ 4H ₂ O + Ca ²⁺ + 2Al ³⁺ + 2SiO _{2(aq)}
Kaolinite + 6H ⁺ ↔ 5H ₂ O + 2Al ³⁺ + 2SiO _{2(aq)}
Muscovite + 6H ⁺ ↔ 6H ₂ O + K ⁺ + 3Al ³⁺ + 3SiO _{2(aq)}
Quartz ↔ SiO _{2(aq)}

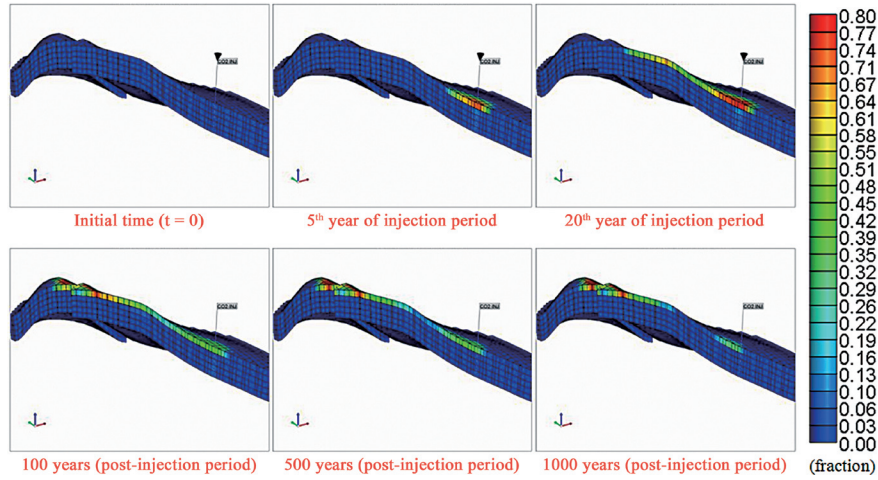


Fig. 5. Plume migration of supercritical phase CO₂ at various times: (a) initial time (the beginning of the injection period), (b) 5 years, (c) 20 years (the end of the injection period), (d) 100 years, (e) 500 years, (f) 1000 years (the end of simulation time).

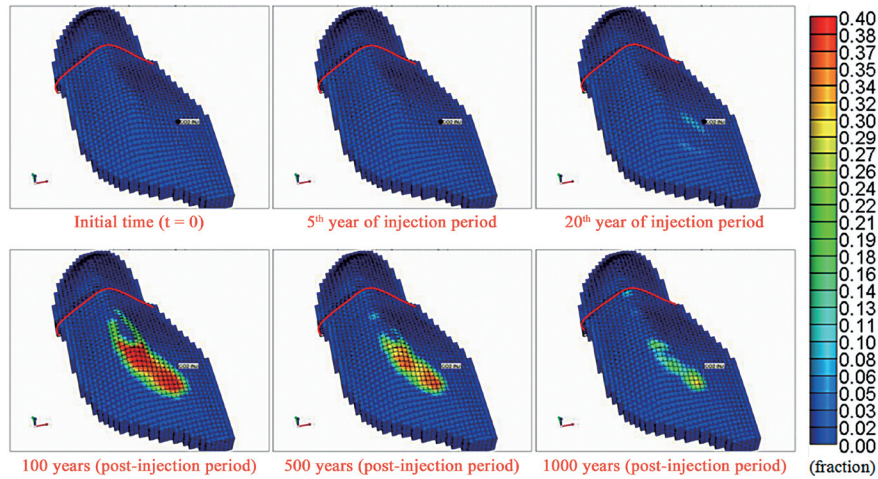


Fig. 6. Immobile supercritical phase (residual) CO₂ spatial distribution at various times: (a) initial time (the beginning of the injection period), (b) 5 years, (c) 20 years (the end of the injection period), (d) 100 years, (e) 500 years, (f) 1000 years (the end of simulation time).

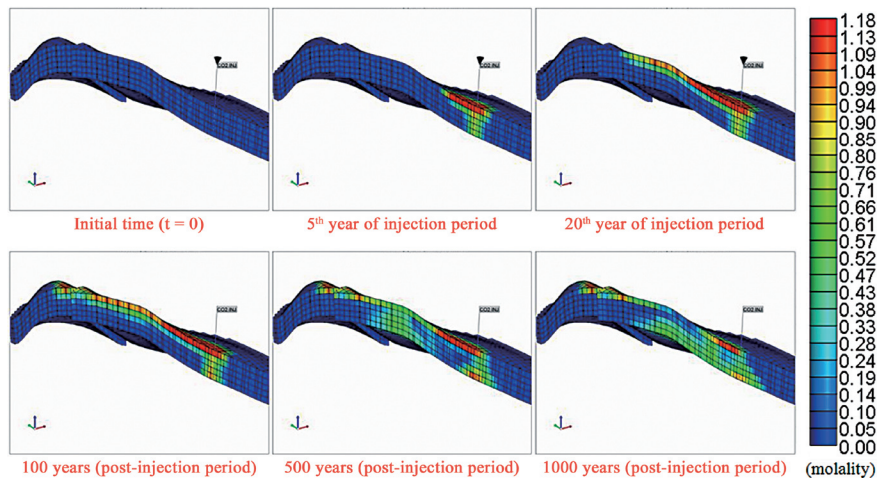


Fig. 7. Aqueous phase CO₂ plume migration at various times: (a) initial time (the beginning of the injection period), (b) 5 years, (c) 20 years (the end of the injection period), (d) 100 years, (e) 500 years, (f) 1000 years (the end of simulation time).

upward to the top of the structure (Figs. 5a - c). During the CO₂ injection period, the difference in migration behavior between the aqueous CO₂ (Fig. 7c) and supercritical CO₂ (Fig. 5c) plumes is easily seen, especially in the vicinity of the wellbore.

In the post-injection period, convection transfers a large amount of aqueous CO₂ to the bottom of the formation. The aqueous CO₂ finally accumulates in the down-dip of the structure (Figs. 7d - f), where it is safe and distant from the cap rock. The plume migration of aqueous CO₂ shows that the risk for CO₂ leakage can be lowered when the solubility trapping mechanism operates continuously.

The simulation results show that the plume migration of ionic CO₂ (HCO₃⁻) (Figs. 8a - f) is very similar to that of aqueous CO₂ (Figs. 7a - f). This is because the ionic CO₂ is formed from the aqueous CO₂ and formation water (H₂O) reaction. In other words, the aqueous CO₂ plume is the cradle for creating ionic phase CO₂. During CO₂ injection the ionic CO₂ (HCO₃⁻) (Figs. 8a - c) plume migration is similar to that of supercritical CO₂ (Figs. 5a - c). The convection effect, which dominates the plume migration of aqueous CO₂, also affects the plume migration of ionic CO₂. In the post-injection period convection causes a large amount of aqueous CO₂ to sink to the bottom of the formation (Figs. 7d - f). Consequently, the ionic CO₂ (HCO₃⁻) plume has the same flow behavior (Figs. 8d - f). Similar to aqueous CO₂, ionic phase CO₂ (HCO₃⁻) tends to sink and accumulate in the down-dip of the structure. Ionic CO₂ is also distant from the cap rock. Based on the simulation results the ionic trapping mechanism changes the phase of CO₂ into a safer ionic phase and generates flow behavior that is low-leakage-risk and allows safe storage.

The precipitation of carbonates is because of the reaction between the ionic CO₂ (HCO₃⁻) and rock minerals. In this case study, anorthite dissolved in the low pH environment yielded calcium (Ca²⁺). Calcite (CaCO₃) was precipitated from the reaction between the bicarbonate (HCO₃⁻) and the calcium (Ca²⁺). Calcite (CaCO₃) is the major mineral phase CO₂ in this case study. Our simulation results show that the pH value of the formation water was lowered after CO₂ was injected into the formation, and that the variations in the kaolinite and muscovite were caused first. A small amount of muscovite was dissolved and kaolinite was precipitated. The simulation results were identical to the observations from the preliminary *GAMSP* theoretical study (GAMS 2011a).

The simulation results show that there is no calcite precipitation during the 20-year injection period (Figs. 9a - c). Moreover, the precipitation of kaolinite and the dissolution of muscovite did not substantially affect the formation porosity. Based on the simulation results, there were almost no changes in formation porosity during the injection period.

In the post-injection period calcite precipitation was the predominant reaction during mineralization. After 100

years a small amount of calcite precipitated into the formation pores where the ionic CO₂ plume had formed (Fig. 9d). The ionic CO₂ plume was the source of the calcite precipitation (Figs. 8e, 9e). The up-dip of the structure was not the major location of mineralization (Fig. 9f) because the source (bicarbonate) of the mineralization tended to sink to the bottom of the structure. Moreover, the dynamic changes in the formation porosity were related to the mineral CO₂ (CaCO₃) spatial distribution. At the end of the simulation (1000 years), the formation porosity had decreased by 0.2% near the wellbore. The wellbore vicinity is where most damage to the formation porosity occurred.

6. DISCUSSION

The flow path and velocity of supercritical CO₂ is essential information for evaluating the AOR and for monitoring and safety in a CO₂ storage project. In this study, the flow path of the supercritical CO₂ was traced and the velocity of the supercritical CO₂ was estimated from the plume front moving distance of supercritical CO₂.

The plume of supercritical CO₂ first moved northwest, turned north-northwest, and accumulated in the up-dip of the structure (Fig. 10). By investigating the plume area at the end of the injection period (Fig. 10), we saw that the average the supercritical CO₂ plume velocity was about 320 m year⁻¹ (1050 ft year⁻¹) or about 0.88 m day⁻¹ (2.9 ft day⁻¹) during the 20-year injection period.

In the post-injection period the supercritical CO₂ velocity slowed because CO₂ was no longer being injected. The trap of the structure restricted supercritical CO₂ plume extension. Based on our results, the area size of the supercritical CO₂ plume was the largest at the simulation time of 60 years (40 years after the end of injection) (Figs. 11a, b). The area size of the supercritical CO₂ was about 13.9 km² (Fig. 11a) and the volume of the supercritical CO₂ was about 0.45 km³ (Fig. 11b). The plume volume was relatively small. The vertical sweep efficiency affected the plume volume because the supercritical CO₂ always flowed on the top of the formation because of its buoyancy (Fig. 11b).

The size of the area and the volume of the aqueous CO₂ were also investigated and compared. The area size of the aqueous CO₂ was about 16.7 km² (Fig. 11c) and the aqueous CO₂ plume volume was about 2.55 km³ (Fig. 11d). At the simulation time of 60 years the size of the aqueous CO₂ plume volume was about 5.7 times larger than that of the supercritical CO₂. This is because convection increased the vertical sweep efficiency, which, in turn, increased the aqueous CO₂ plume volume.

7. CONCLUSIONS

The mobile supercritical CO₂ plume first moves upward because of its buoyancy, and then flows under the

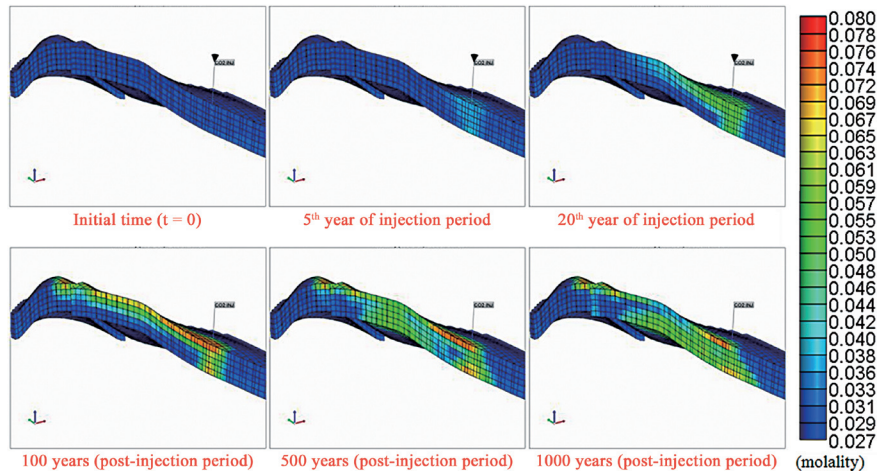


Fig. 8. Ionic phase CO₂ (HCO₃⁻) plume migration at various times: (a) initial time, (b) 5 years, (c) 20 years (or the end of the injection period), (d) 100 years, (e) 500 years, (f) 1000 years (or the end of simulation time).

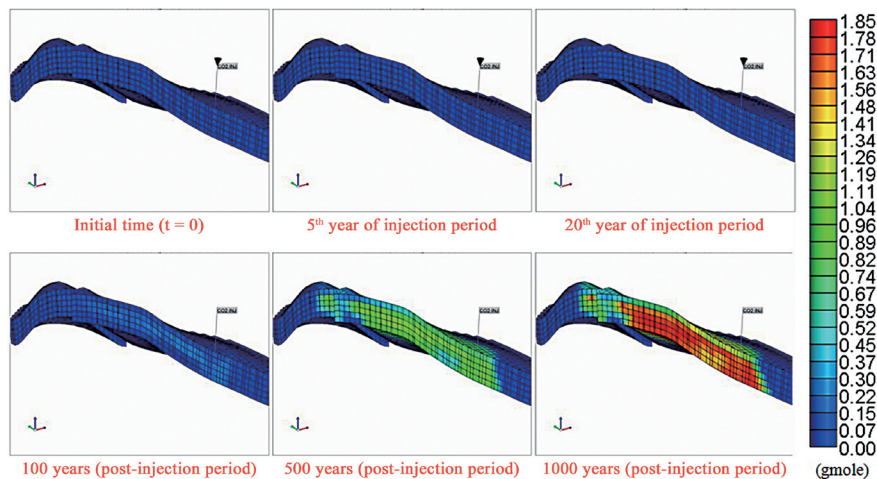


Fig. 9. Mineral (solid) phase CO₂ (CaCO₃) spatial distribution at various times: (a) initial time (the beginning of the injection period), (b) 5 years, (c) 20 years (the end of the injection period), (d) 100 years, (e) 500 years, (f) 1000 years (the end of simulation time).

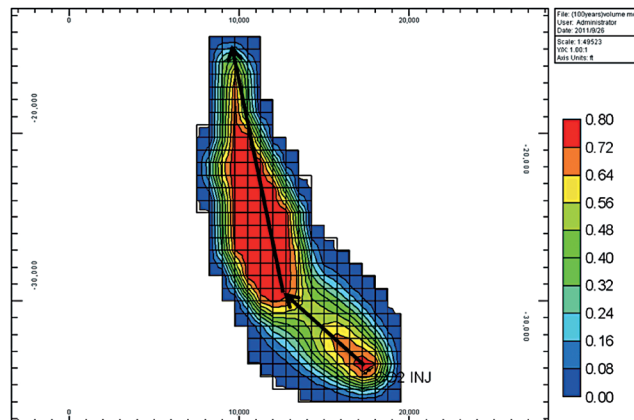


Fig. 10. Supercritical phase CO₂ flow path and plume area at the end of the CO₂ injection period (or the simulation time of 20 years).

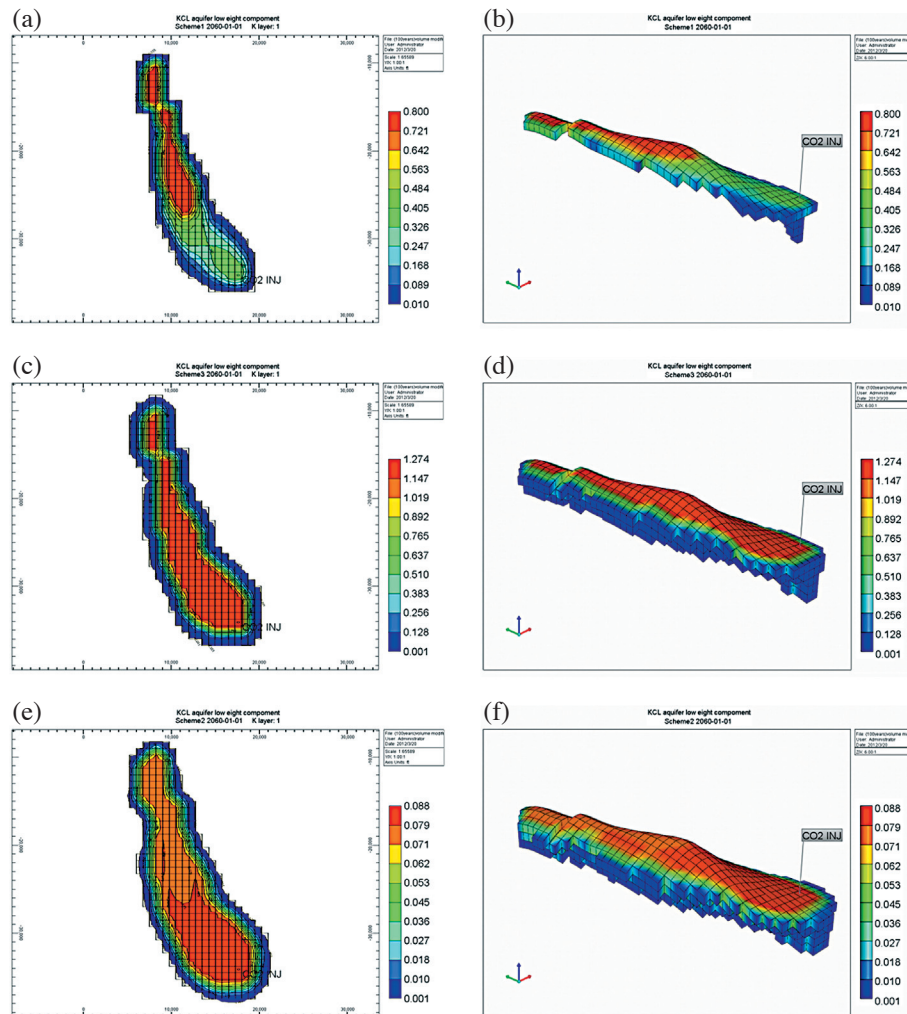


Fig. 11. Supercritical phase CO₂ and aqueous phase CO₂ plume area and volume at the simulation time of 60 years: (a) plume area of supercritical phase CO₂, (b) plume volume of supercritical phase CO₂, (c) plume area of aqueous phase CO₂, (d) plume volume of aqueous phase CO₂.

impermeable cap rock. In this case study, the average velocity of the supercritical CO₂ plume was about 0.88 m day⁻¹ during the 20-year injection period.

Supercritical CO₂ will become immobile at the rear of the moving plume due to imbibition. In the post-injection period, the quantity of the residual CO₂ reached a maximum and then became smaller because of the solubility trapping mechanism. Residual gas trapping is a fast and safe mechanism for trapping injected CO₂.

The plume size of aqueous CO₂ is larger than that of supercritical CO₂. In this study the aqueous CO₂ plume volume was about 5.7 times larger than that of the supercritical CO₂ at the simulation time of 60 years because convection increased the vertical sweep efficiency.

Convection causes ionic CO₂ to accumulate in the down-dip of the structure and distant from the cap rock. The ionic trapping mechanism changes the CO₂ into a safer ionic phase and also generates flow behavior that is low-leakage-risk and allows safe storage.

The up-dip of the structure was not the major mineralization location, because the source (bicarbonate) of the mineralization tended to sink to the down-dip of the structure.

Acknowledgements This work was supported by grant MOST 103-2221-E-006-223-MY2 from the Ministry of Science and Technology, Taiwan. The authors wish to thank CPC Corporation, Taiwan for providing the analysis data for the geological properties, reservoir properties, and rock and fluid samples.

REFERENCES

- Bachu, S., 2003: Screening and ranking of sedimentary basins for sequestration of CO₂ in geological media in response to climate change. *Environ. Geol.*, **44**, 277-289, doi: 10.1007/s00254-003-0762-9. [Link]
- Bachu, S., 2008: CO₂ storage in geological media: Role, means, status and barriers to deployment. *Prog. Energ.*

- Combust.*, **34**, 254-273, doi: 10.1016/j.pecs.2007.10.001. [[Link](#)]
- Bachu, S., W. D. Gunter, and E. H. Perkins, 1994: Aquifer disposal of CO₂: Hydrodynamic and mineral trapping. *Energ. Convers. Manage.*, **35**, 269-279, doi: 10.1016/0196-8904(94)90060-4. [[Link](#)]
- Bakker, R. J., 2003: Package *FLUIDS* 1. Computer programs for analysis of fluid inclusion data and for modelling bulk fluid properties. *Chem. Geol.*, **194**, 3-23, doi: 10.1016/S0009-2541(02)00268-1. [[Link](#)]
- Bennion, B. and S. Bachu, 2005: Relative permeability characteristics for supercritical CO₂ displacing water in a variety of potential sequestration zones. SPE Annual Technical Conference and Exhibition, Society of Petroleum Engineers, Dallas, Texas, doi: 10.2118/95547-MS. [[Link](#)]
- Bethke, C. M., 1996: *Geochemical Reaction Modelling: Concept and Applications*, Oxford University Press, New York, 416 pp.
- CMG (Computer Modelling Group), 2011a: GEM Advanced Compositional and GHG Reservoir Simulator, User's Guide, Computer Modelling Group Ltd., Calgary, Alberta.
- CMG (Computer Modelling Group), 2011b: WinProp Phase Property Program, User's Guide, Computer Modelling Group Ltd., Calgary, Alberta.
- CPC, 2010: Simulation Study of Carbon Dioxide Geological Sequestration in Depleted Gas Reservoir, CPC Corporation, Taiwan, Cooperative Education Technical Report (Project number: FEB-9914001). (in Chinese)
- Delaney, J. M. and S. R. Lundeen, 1990: The LLNL Thermochemical Database, Report UCRL-21658, Lawrence Livermore National Laboratory, Livermore, Calif.
- Ennis-King, J. P. and L. Paterson, 2005: Role of convective mixing in the long-term storage of carbon dioxide in deep saline formations. *Soc. Petrol. Eng. J.*, **10**, 349-356, doi: 10.2118/84344-PA. [[Link](#)]
- EPA (Environmental Protection Agency), 2014: Glossary in United States Environmental Protection Agency (US EPA) website. Available at <http://water.epa.gov/type/groundwater/uic/glossary.cfm>.
- Flett, M., R. Gurton, and I. Taggart, 2004: The function of gas-water relative permeability hysteresis in the sequestration of carbon dioxide in saline formations. SPE Asia Pacific Oil and Gas Conference and Exhibition, Perth, Australia, doi: 10.2118/88485-MS. [[Link](#)]
- GAMS (General Algebraic Modeling System), 2011a: Gamspath Geochemical Reaction Path Models, Geochemical Applications & Modelling Software Ltd., Edmonton, Alberta.
- GAMS (General Algebraic Modeling System), 2011b: Solmineq.88 Geochemical Aqueous Equilibrium Models, Geochemical Applications & Modelling Software Ltd., Edmonton, Alberta.
- Garcia, J. E., 2001: Density of Aqueous Solutions of CO₂, Report LBNL-49023, Lawrence Berkeley National Laboratory.
- Gaus, I., M. Azaroual, and I. Czernichowski-Lauriol, 2005: Reactive transport modelling of the impact of CO₂ injection on the clayey cap rock at Sleipner (North Sea). *Chem. Geol.*, **217**, 319-337, doi: 10.1016/j.chem-geo.2004.12.016. [[Link](#)]
- Gunter, W. D., B. Wiwchar, and E. H. Perkins, 1997: Aquifer disposal of CO₂-rich greenhouse gases: Extension of the time scale of experiment for CO₂-sequestering reactions by geochemical modelling. *Miner. Petrol.*, **59**, 121-140, doi: 10.1007/BF01163065. [[Link](#)]
- Gunter, W. D., S. Bachu, and S. Benson, 2004: The role of hydrogeological and geochemical trapping in sedimentary basins for secure geological Storage of carbon dioxide. *Geol. Soc. Lond. Spec. Publ.*, **233**, 129-145, doi: 10.1144/GSL.SP.2004.233.01.09. [[Link](#)]
- Gunter, W. D., S. Talman, and E. Perkins, 2008: Geosequestration geochemistry. Proceedings of 2008 Asia Pacific Coalbed Methane Symposium, 22-24 September 2008, Brisbane, Queensland.
- Harvey, A. H., 1996: Semiempirical correlation for Henry's constants over large temperature ranges. *AIChE J.*, **42**, 1491-1494, doi: 10.1002/aic.690420531. [[Link](#)]
- Hsieh, B. Z., L. Nghiem, C. H. Shen, and Z. S. Lin, 2013: Effects of complex sandstone-shale sequences of a storage formation on the risk of CO₂ leakage: Case study from Taiwan. *Int. J. Greenh. Gas Con.*, **17**, 376-387, doi: 10.1016/j.ijggc.2013.05.030. [[Link](#)]
- Ide, S. T., K. Jessen, and F. M. Orr Jr., 2007: Storage of CO₂ in saline aquifers: Effects of gravity, viscous, and capillary forces on amount and timing of trapping. *Int. J. Greenh. Gas Con.*, **1**, 481-491, doi: 10.1016/S1750-5836(07)00091-6. [[Link](#)]
- IEA (International Energy Agency), 2008: CO₂ Capture and Storage - A Key Carbon Abatement Option.
- IPCC (Intergovernmental Panel on Climate Change), 2005: Carbon Dioxide Capture and Storage: Special Report of the Intergovernmental Panel on Climate Change, Cambridge University Press, New York, 431 pp.
- Juanes, R., E. J. Spiteri, F. M. Orr Jr., and M. J. Blunt, 2006: Impact of relative permeability hysteresis on geological CO₂ storage. *Water Resour. Res.*, **42**, W12418, doi: 10.1029/2005WR004806. [[Link](#)]
- Kharaka, Y. K., W. D. Gunter, P. K. Aggarwal, E. H. Perkins, and J. D. Debraal, 1988: Solmineq.88: A Computer Program for Geochemical Modeling of Water-Rock Interactions, Water-Resources Investigations Report 88-4227, U.S. Geological Survey, Menlo Park, California.
- Kumar, A., M. H. Noh, R. C. Ozah, G. A. Pope, S. L. Bryant, K. Sepehrnoori, and L. W. Lake, 2005: Reservoir simulation of CO₂ storage in aquifers. *Soc. Petrol. Eng.*

- J.*, **10**, 336-348, doi: 10.2118/89343-PA. [[Link](#)]
- Land, C. S., 1968: Calculation of imbibition relative permeability for two- and three-phase flow from rock properties. *Soc. Petrol. Eng. J.*, **8**, 149-156, doi: 10.2118/1942-PA. [[Link](#)]
- Li, Y. K. and L. X. Nghiem, 1986: Phase equilibria of oil, gas and water/brine mixtures from a cubic equation of state and Henry's Law. *Can. J. Chem. Eng.*, **64**, 486-496, doi: 10.1002/cjce.5450640319. [[Link](#)]
- Lin, A. T., 2001: Cenozoic stratigraphy and tectonic development of the west Taiwan basins. Ph.D. Thesis, University of Oxford, Oxford, UK.
- Lin, A. T., A. B. Watts, and S. P. Hesselbo, 2003: Cenozoic stratigraphy and subsidence history of the South China Sea margin in the Taiwan region. *Basin Res.*, **15**, 453-478, doi: 10.1046/j.1365-2117.2003.00215.x. [[Link](#)]
- Lin, C. K., 2007: The optimum sequestration depth for CO₂ geo-sequestration. 9th International Conference on Gas Geochemistry, Taipei.
- Nghiem, L., P. Sammon, J. Grabenstetter, and H. Ohkuma, 2004: Modeling CO₂ storage in aquifers with a fully-coupled geochemical EOS compositional simulator. SPE/DOE Symposium on Improved Oil Recovery, Tulsa, Oklahoma, doi: 10.2118/89474-MS. [[Link](#)]
- Nghiem, L., V. Shrivastava, B. Kohse, M. Hassam, and C. Yang, 2009a: Simulation of trapping processes for CO₂ storage in saline aquifers. Canadian International Petroleum Conference, Calgary, Alberta, doi: 10.2118/2009-156. [[Link](#)]
- Nghiem, L., V. K. Shrivastava, D. Tran, B. F. Kohse, M. S. Hassam, and C. Yang, 2009b: Simulation of CO₂ storage in saline aquifers. SPE/EAGE Reservoir Characterization and Simulation Conference, Abu Dhabi, UAE, doi: 10.2118/125848-MS. [[Link](#)]
- Nghiem, L., C. Yang, V. K. Shrivastava, B. F. Kohse, M. S. Hassam, D. Chen, and C. Card, 2009c: Optimization of residual gas and solubility trapping for CO₂ sequestration in saline aquifers. SPE Reservoir Simulation Symposium, Woodlands, Texas, doi: 10.2118/119080-MS. [[Link](#)]
- Nicot, J. P., C. M. Oldenburg, S. L. Bryant, and S. D. Hovorka, 2008: Pressure perturbations from geologic carbon sequestration: Area-of-review boundaries and borehole leakage driving forces. GHGT9 Conference, LBNL Paper LBNL-3064E, Washington, DC.
- Peng, D. Y. and D. B. Robinson, 1976: A new two-constant equation of state. *Ind. Eng. Chem. Fundamen.*, **15**, 59-64, doi: 10.1021/i160057a011. [[Link](#)]
- Pitzer, K. S., 1987: A thermodynamic model for aqueous solutions of liquid-like density. *Rev. Mineral. Geochem.*, **17**, 97-142.
- Pruess, K., T. Xu, J. Apps, and J. Garcia, 2003: Numerical modeling of aquifer disposal of CO₂. *Soc. Petrol. Eng. J.*, **8**, 49-60, doi: 10.2118/83695-PA. [[Link](#)]
- Qi, R., T. C. LaForce, and M. J. Blunt, 2009: Design of carbon dioxide storage in aquifers. *Int. J. Greenh. Gas Con.*, **3**, 195-205, doi: 10.1016/j.ijggc.2008.08.004. [[Link](#)]
- Rochelle, C. A., I. Czernichowski-Lauriol, and A. E. Milodowski, 2004: The impact of chemical reactions on CO₂ storage in geological formations: A brief review. *Geol. Soc. Lond. Spec. Publ.*, **233**, 87-106, doi: 10.1144/GSL.SP.2004.233.01.07. [[Link](#)]
- Shaw, C. L., 1996: Stratigraphic correlation and isopach maps of the western Taiwan basin. *Terr. Atmos. Ocean. Sci.*, **7**, 333-360.
- Thibeau, S., L. X. Nghiem, and H. Ohkuma, 2007: A modelling study of the role of selected minerals in enhancing CO₂ mineralization during CO₂ aquifer storage. SPE Annual Technical Conference and Exhibition, Anaheim, California, U.S.A., doi: 10.2118/109739-MS. [[Link](#)]
- Wu, J. C., W. R. Chi, M. H. Wang, C. C. Tsia, Y. Y. Lee, and C. C. Chang, 2005: The study of nannoplankton biostratigraphy and paleoenvironments in Peikang area southwestern Taiwan, Annual Meeting of Geological Society, Taipei. (in Chinese)
- Xu, T., J. A. Apps, and K. Pruess, 2004: Numerical simulation of CO₂ disposal by mineral trapping in deep aquifers. *Appl. Geochem.*, **19**, 917-936, doi: 10.1016/j.apgeochem.2003.11.003. [[Link](#)]